Use of segmented constrained layer damping treatment for improved helicopter aeromechanical stability

Smart Mater. Struct. **9** (2000) 523–532. Printed in the UK PII: S0964-1726(00)13963-1

Use of segmented constrained layer damping treatment for improved helicopter aeromechanical stability

Qiang Liu, Aditi Chattopadhyay, Haozhong Gu† and Xu Zhou

Department of Mechanical and Aerospace Engineering, Arizona State University, Tempe, AZ 85287-6106, USA

Received 17 September 1999, in final form 20 April 2000

Abstract. The use of a special type of smart material, known as segmented constrained layer (SCL) damping, is investigated for improved rotor aeromechanical stability. The rotor blade load-carrying member is modeled using a composite box beam with arbitrary wall thickness. The SCLs are bonded to the upper and lower surfaces of the box beam to provide passive damping. A finite-element model based on a hybrid displacement theory is used to accurately capture the transverse shear effects in the composite primary structure and the viscoelastic and the piezoelectric layers within the SCL. Detailed numerical studies are presented to assess the influence of the number of actuators and their locations for improved aeromechanical stability. Ground and air resonance analysis models are implemented in the rotor blade built around the composite box beam with segmented SCLs. A classic ground resonance model and an air resonance model are used in the rotor–body coupled stability analysis. The Pitt dynamic inflow model is used in the air resonance analysis under hover condition. Results indicate that the surface bonded SCLs significantly increase rotor lead-lag regressive modal damping in the coupled rotor–body system.

1. Introduction

Aeromechanical stability is a key issue in helicopter design and lead-lag modal damping is an important parameter in this analysis. To ensure helicopter stability in normal operation, adequate rotor damping and body damping are necessary, which are produced mainly from rotor dampers and fuselage landing gears. The object of this paper is to investigate the use of a special type of smart material for improved rotorcraft aeromechanical stability.

The use of smart materials and active control technology for helicopter vibratory load reduction has been investigated by several researchers [1–6]. Two principal strategies have been investigated for reducing rotor dynamic loads. The first is controllable twist blades with embedded piezoceramics [1, 3]. The second is trailing edge flaps actuated with piezobimorphs [4]. An integrated analytical procedure was developed by Chattopadhyay *et al* [5, 6] using a smart composite box beam structural dynamic model and a finite state induced inflow model [7] to investigate vibratory load reduction at the rotor hub. Significant load reductions and improvements in the rotor response were observed with closed loop control.

Recently, the concept of an active constrained layer (ACL) damping treatment was proposed by Baz and Ro [8, 9] and Ro and Baz [10]. An ACL configuration comprises a piezoelectric layer (PZT) and a viscoelastic bonding layer that connects the piezoelectric layer to the surface of the primary structure. A considerable amount of research has been performed in modeling ACL, as summarized in [8–10]. It is well known that a segmented constraining layer (SCL) is an effective means of increasing the passive damping in long wavelength vibration modes, such as fundamental rotor blade lead-lag mode, by increasing the number of high shear regions. Lesieutre and Lee [11] explored the segmented configuration in the ACL damping treatment. However, the SCLs presented in their paper still cover the entire surface of the structure and do not represent a realistic configuration for engineering practice. The primary concern in such a configuration is the concept that the actuation ability of the piezoelectric layer is reduced by the viscoelastic layer. However, the ACL (piezoelectric layer) increases the shear deformation in the viscoelastic layer and therefore, in reality, forms an effective means of enhancing the damping mechanism. Recently, an enhanced active constrained layer (EACL) model was developed by Badre-Alam *et al* [12] and Liu and Wang [13] in which a pair of stiff edge elements at the edge of the PZT layer was added to provide a parallel load path to the host structure. This leads to improved control authority. However, in the open-loop, the shear transmissibility from PZT to the host structure can be reduced as a result of the multiple load paths. Since a part of the load is transferred directly from the PZT layer to the host structure via the stiff edge elements, this could result in

† Present address: Design, Manufacturing and Producibility Simulation, The Boeing Company, PO Box 516 MC S064-2809, St Louis, MO 63166-0516, USA.

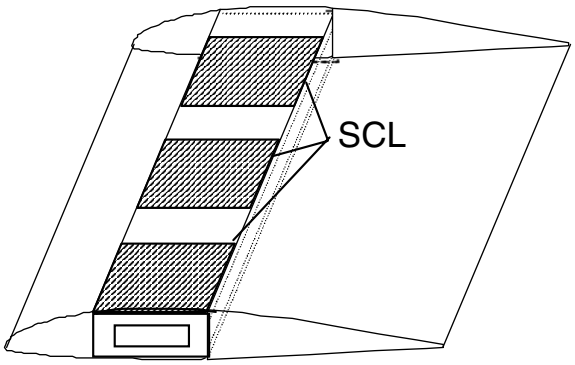

Figure 1. Rotary wing with SCLs.

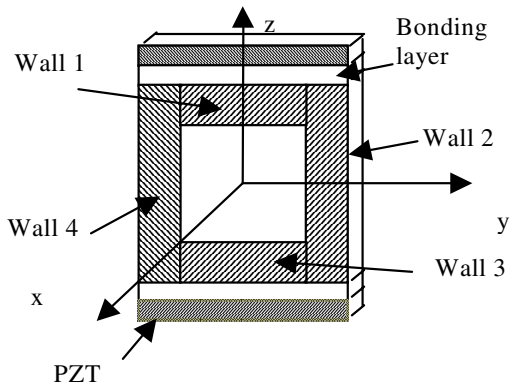

Figure 2. Illustration of the box beam element and walls.

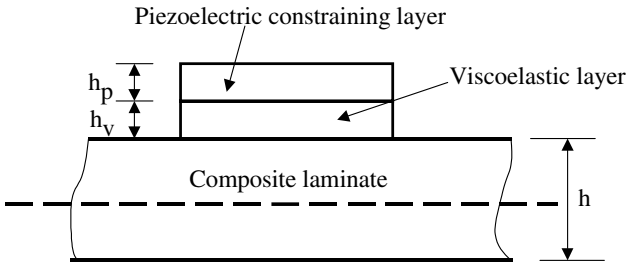

Figure 3. Composite with a SCL.

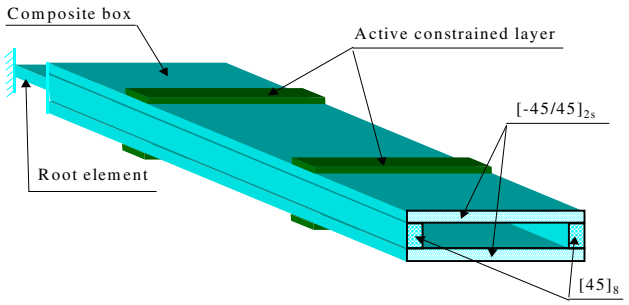

Figure 4. Composite box beam configuration.

reduced modal damping. Also, for practical implementation, the possible debonding between the edge elements and the ACL is an important issue that needs to be addressed. The model was implemented in the flex beam of a rotor blade to enhance aeromechanical stability [12]. A comprehensive and practical approach to modeling the sparse sequenced ACL damping treatment on composite plates of arbitrary thickness was recently developed by Gu *et al* [14]. In this work, a hybrid displacement theory was developed to efficiently model the transverse shear stresses in the various material layers. Since the SCL configuration capitalizes on both passive and active damping techniques in a synergistic manner, it has been shown to be an effective method for vibration suppression in composite structures [13].

The object of this paper is to investigate the use of the SCL passive damping treatment for improved helicopter aeromechanical stability. A classical ground resonance model and an air resonance model are used to investigate the coupled rotor–body stability. Parametric studies are conducted to observe the effect of the spanwise location and number of SCLs on rotor lead-lag modal damping.

2. Structural modeling

The principal rotor load-carrying member is represented by a composite box beam of arbitrary wall thickness. The SCLs are surface bonded to the top and bottom surfaces of the box beam (figure 1). The box beam is modeled using composite laminates representing the four walls (figure 2). Since a SCL comprises a piezoelectric layer and a viscoelastic bonding layer (figure 3), it is necessary to accurately model the displacement fields, the boundary and the continuity conditions between the different layers.

A new hybrid displacement theory was recently developed by Gu *et al* [14] to model a surface bonded SCL on a composite plate (figure 3). This plate model is now extended to develop a finite-element model for the analysis of the composite box beam with a surface bonded SCL damping treatment. The theory uses a higher-order displacement field to capture the transverse shear effects in the composite primary structure. Since viscoelastic and piezoelectric layers are made from isotropic material, the first and second order displacement fields are employed in these layers to maintain computational efficiency. The refined displacement fields, defined in the three different material layers, are derived by applying the displacement and transverse shear stress continuity conditions at the layer interfaces, and the traction-free boundary conditions on the top and the bottom surfaces of the structure.

Based on the refined displacement field assumption [14], the total strain vector for an element with a viscoelastic damping layer and a piezoelectric actuator layer can be expressed as follows:

$$\varepsilon = \begin{cases} \varepsilon_c & -h_i/2 \leqslant z^i \leqslant h_i/2 \\ \varepsilon_v & h_i/2 \leqslant z^i \leqslant h_i/2 + h_v \\ \varepsilon_p & h_i/2 + h_v \leqslant z^i \leqslant h_i/2 + h_v + h_p \end{cases} \qquad (x^i, y^i) \in \Sigma_2 \tag{1}$$

where the subscripts c, v and p denote variables defined in the composite region, viscoelastic region and piezoelectric region only. Quantities ε_c, ε_v and ε_p represent the strains in the three different material layers, (x^i, y^i, z^i) represents a point in the local coordinate of the ith wall ($i = 1$–4) and Σ_2 represents the layer area. Quantities h_v and h_p represent the thickness of viscoelastic layer and piezoelectric layer, respectively, and h_i is the thickness of the composite layer in the ith wall.

In the hybrid displacement theory each wall of the box beam is separated through the thickness into three different regions: composite region (region c), viscoelastic region (region v) and piezoelectric region (region p). The following refined displacement field is obtained after satisfaction of the boundary conditions:

$$u^c = u_0^c - zw_{0,x}^c + z\left(1 - \frac{4z^2}{3h^2}\right)\psi_x^c + \frac{2z^2}{3h^2}\left(z + \frac{3}{4}h\right)\frac{G^v}{G_{13}^c}\psi_x^v$$

$$v^c = v_0^c - zw_{0,y}^c + z\left(1 - \frac{4z^2}{3h^2}\right)\psi_y^c + \frac{2z^2}{3h^2}\left(z + \frac{3}{4}h\right)\frac{G^v}{G_{23}^c}\psi_y^v$$

$$w^c = w_0^c \qquad \text{where } -\frac{h}{2} \leqslant z \leqslant \frac{h}{2} \tag{2a}$$

$$u^v = u_0^c + \frac{h}{3}\psi_x^c - zw_{0,x}^c + \left(z - \frac{h}{2} + \frac{5h}{24}\frac{G^v}{G_{13}^c}\right)\psi_x^v$$

$$v^v = v_0^c + \frac{h}{3}\psi_y^c - zw_{0,y}^c + \left(z - \frac{h}{2} + \frac{5h}{24}\frac{G^v}{G_{23}^c}\right)\psi_y^v$$

$$w^v = w_0^c \qquad \text{where } \frac{h}{2} \leqslant z \leqslant \frac{h}{2} + h_v \tag{2b}$$

$$u^p = u_0^c + \frac{h}{3}\psi_x^c - zw_{0,x}^c + \left(\frac{G^v}{G^p}\frac{1}{2h_p}(2h_4 z - z^2 - h_3h_4 - h_3h_p) + h_v + \frac{5h}{24}\frac{G^v}{G_{13}^c}\right)\psi_x^v$$

$$v^p = v_0^c + \frac{h}{3}\psi_y^c - zw_{0,y}^c + \left(\frac{G^v}{G^p}\frac{1}{2h_p}(2h_4 z - z^2 - h_3h_4 - h_3h_p) + h_v + \frac{5h}{24}\frac{G^v}{G_{23}^c}\right)\psi_y^v$$

$$w^p = w_0^c \qquad \text{where } \frac{h}{2} + h_v \leqslant z \leqslant \frac{h}{2} + h_v + h_p \tag{2c}$$

with

$$h_3 = \frac{h}{2} + h_v \qquad h_4 = \frac{h}{2} + h_v + h_p \tag{3}$$

where u, v and w are the in-plane and the out-of-plane displacements at a point (x, y, z); u_0, v_0 and w_0 represent the displacements at the midplane, ψ_x and ψ_y represent the rotations of the normals to the midplane; and G is the shear modulus of the material. The present approach is able to capture the varying behaviors in the different material regions. It also has the advantage of introducing fewer additional unknown variables (only two additional variables, ψ_x^v and ψ_y^v, compared to those in the regular refined third-order theory) while satisfying all boundary and continuity conditions. In addition, an added benefit is that the boundary conditions for the two additional unknowns, ψ_x^v and ψ_y^v, defined in a SCL, can also be derived using the present approach. To determine these two additional unknowns, the regular refined third-order displacement field used in section 1 (section without viscoelastic layer and the piezoelectric constraining layer) is presented:

$$u_1^c = u_0^c - zw_{0,x}^c + z\left(1 - \frac{4z^2}{3h^2}\right)\psi_x^c + \frac{2z^2}{3h^2}\left(z + \frac{3}{4}h\right)\frac{G^v}{G_{13}^c}\psi_x^v$$

$$u_2^c = v_0^c - zw_{0,y}^c + z\left(1 - \frac{4z^2}{3h^2}\right)\psi_y^c + \frac{2z^2}{3h^2}\left(z + \frac{3}{4}h\right)\frac{G^v}{G_{23}^c}\psi_y^v$$

$$u_3^c = w_0^c \qquad \text{where } -\frac{h}{2} \leqslant z \leqslant \frac{h}{2}. \tag{4}$$

The continuity conditions at the section interface require that the displacements defined in adjacent section (equations (2) and (4)) are equal to each other through the thickness. These lead to

$$\psi_x^v(x, y) = \psi_y^v(x, y) = 0 \qquad (x, y) \in \Gamma_s \tag{5}$$

where Γ_s represents the section interface.

The finite-element equations for each wall are derived using the discretized form of Hamilton's principle. The variation of kinetic energy (δK) for a laminate, representing a wall with rotation can be expressed as

$$\begin{aligned}\delta K = &\int_A \int_z \rho[\delta(\dot{u} + \Omega \times (r_0 + u))] \\ &\cdot(\dot{u} + \Omega \times (r_0 + u))\,\mathrm{d}z\,\mathrm{d}A \\ = &-\int_A \int_z \rho\delta u[\ddot{u} + 2\Omega \times \dot{u} + \Omega \times (\Omega \times (r_0 + u)) \\ &-(r_0 + u) \times (\Omega \times \Omega)]\,\mathrm{d}z\,\mathrm{d}A\end{aligned} \tag{6}$$

where A denotes the surface area of the wall, u is the total displacement vector, Ω is the angular velocity vector, ρ is the mass density and r_0 denotes the distance from center point of rotation axis to the measured point of the original configuration. The overdot denotes differentiation with respect to time, t.

The centrifugal contribution, which contains no displacement variables in equation (6), can be defined as a centrifugal force (f_c). The centrifugal force causes the initial stress σ_0 in the structure, which finally constitutes the partial centrifugal stiffening matrix incorporated with the structural rotation ω:

$$f_c = \int_A \int_z \rho(\Omega \times (\Omega \times r_0) - r_0 \times (\Omega \times \Omega))\,\mathrm{d}z\,\mathrm{d}A. \tag{7}$$

Equation (6) can now be expressed as

$$\delta K = -\int_A \int_z [\rho\delta u^T(\ddot{u} + D_g\dot{u} + D_c u) + \delta\omega^T\sigma_0\omega]\,\mathrm{d}z\,\mathrm{d}A \tag{8}$$

where D_g and D_c are the gyroscopic coupling coefficient and the centrifugal stiffening coefficient, respectively.

The variation of elastic strain energy (δU) can be expressed as

$$\delta U = \int_A \int_z \delta\varepsilon^T \bar{Q}(\varepsilon - \Lambda - \varepsilon_a^v)\,\mathrm{d}z\,\mathrm{d}A \tag{9}$$

where $\bar{Q}$ is the material stiffness, Λ is the piezoelectric induced strain vector and ε_a^v is the anelastic strain vector for the viscoelastic layer. The variation of external work (δW) can be expressed as

$$\delta W = \int_A \delta u^T q \, \mathrm{d}A \tag{10}$$

where q is the applied external distributed force on the box beam wall surfaces. The equations of motion for the ith wall in the local coordinate (x^i, y^i, z^i), are expressed as

$$\begin{aligned}\delta\Pi &= \int_t (\delta K - \delta U - \delta W)\,\mathrm{d}t \\ &= \int_t \int_A \int_z = [\rho\delta u^T(\ddot{u} + D_g\dot{u} + D_c u) + \delta\omega^T\sigma_0\omega \\ &\quad -\delta\varepsilon^T\bar{Q}(\varepsilon - \Lambda - \varepsilon_v^a)]\,\mathrm{d}t - \int_t \int_A \delta u^T q \,\mathrm{d}A\,\mathrm{d}t = 0. \end{aligned}\tag{11}$$

For the wall with a segmented viscoelastic layer and a piezoelectric constraining layer, the anelastic displacement field method [14] is used to implement the viscoelastic material model. This enables time domain finite-element analysis. In this approach, the total deformation (both normal and shear) defined in the viscoelastic material is divided into two parts: (a) the elastic part, in which the strain is instantaneously proportional to the stress and (b) the anelastic part, which captures the characteristic relaxation behavior. That is,

$$u_v = u_v^e + u_v^a \tag{12}$$

where u_v, u_v^e and u_v^a are the total displacement vector, the elastic component and the anelastic component in the viscoelastic layer, respectively. Therefore, the total strain (ε_v) can also be divided into an elastic part (ε_v^e) and an anelastic part (ε_v^a):

$$\varepsilon_v = \varepsilon_v^e + \varepsilon_v^a. \tag{13}$$

It must be noted that in Hamilton's principle only elastic strain ($\varepsilon - \Lambda - \varepsilon_v^a$) can be used.

The general form of the governing equations for the ith wall in its local coordinate, can be expressed as

$$M^i\ddot{u}^i + C_g^i\dot{u}^i + (K^i + K_s^i)u^i = F^i \tag{14}$$

where M^i, K^i, u^i and F^i denote the mass matrix, the stiffness matrix, the nodal displacement vector and the external force vector for the ith wall, respectively. The matrix C_g^i is a gyroscopic damping matrix and K_s^i is the additional stiffness matrix due to centrifugal stiffening, which is expressed by the last two terms on the right-hand side of equation (6).

For the wall with a SCL, the total displacement vector (u) is divided into two parts, the discretized displacement vector (u_g^i) which represents the wall displacement including the composite, the viscoelastic layer and the piezoelectric layer, and the anelastic displacement vector (u_a) pertaining to the viscoelastic layer:

$$u = \begin{Bmatrix} u_g \\ u_a \end{Bmatrix}. \tag{15}$$

Equation (14) can be expressed as follows if gyroscopic damping is neglected:

$$M_g^i\ddot{u}_g^i + K_g^i u_g^i - K_{gv}^i u_a^i = F_g^i \tag{16}$$

where K_{gv}^i is the additional wall global stiffness matrix due to the anelastic strain component.

It is now necessary to derive the equations of motion for the box beam element by combining the four walls. Since the displacement field (defined for an individual wall) takes into account the eccentricity effects, the generally employed coordinate transfer technique is no longer necessary. Due to the hybrid displacement field used [11], deformation continuity conditions (displacements and slopes) are imposed at the intersection of the walls [18] (figure 2).

Using a standard finite-element technique, the governing equations are expressed as

$$M_g\ddot{u}_g + K_g u_g - K_{gv}u_v = F_g \tag{17}$$

where M_g and K_g are the structural global mass and stiffness matrices, respectively, and K_{gv} is the additional structural global stiffness matrix due to the anelastic displacement vector (u_v).

An additional set of ordinary differential equations [18] that describes the time evolution of the anelastic displacement field is employed to obtain the solution of the entire system:

$$\frac{c}{\Omega_d}K_v\dot{u}_v - K_{vg}u_g + cK_v u_v = 0 \tag{18}$$

where K_v is the global stiffness matrix constituting anelastic strain, c is the material constitutive coupling parameter and Ω_d is the characteristic relaxation time at constant strain. The final global equations of motion for the box beam with SCLs can be written as

$$\begin{aligned}&\begin{bmatrix} M_g & 0 \\ 0 & 0 \end{bmatrix}\begin{Bmatrix} \ddot{u}_g \\ \ddot{u}_v \end{Bmatrix} + \begin{bmatrix} 0 & 0 \\ 0 & \frac{c}{\Omega_d}K_v \end{bmatrix}\begin{Bmatrix} \dot{u}_g \\ \dot{u}_v \end{Bmatrix} \\ &\quad + \begin{bmatrix} K_g & -K_{gv} \\ -K_{gv}^T & cK_v \end{bmatrix}\begin{Bmatrix} u_g \\ u_v \end{Bmatrix} = \begin{Bmatrix} F_g \\ 0 \end{Bmatrix}\end{aligned}\tag{19}$$

where F_g is the aerodynamic force vector, which will be explained in a later section. Seven coupled modes are included in this analysis. These include three lead-lag modes, three flap modes and one torsion mode.

3. Ground and air resonance analyses

A classical ground resonance model [19] is shown in figure 5. In this model, only the fundamental lead-lag mode is taken into account. The fuselage is modeled as an equivalent mass, damper and spring system located at the hub center as shown in figure 5. The lateral and longitudinal equivalent mass (M_{fx}, M_{fy}), stiffness (K_{fx}, F_{fy}) and damping (C_{fx}, C_{fy}) matrices represent the lateral and longitudinal fuselage modal characteristics. The values of these parameters are presented in appendix A. Multiblade coordinates are used to transfer rotating coordinates into non-rotating coordinates. The variable ξ_k is the lead-lag displacement of the kth blade. Based on this model, the lead-lag dynamic equation of the kth blade can be expressed as

$$\ddot{\xi}_k + 2\eta\bar{\omega}_\xi\dot{\xi}_k + \bar{\omega}_\xi^2\xi_k + \frac{S_\xi}{I_\xi}(\ddot{\bar{X}}\sin\psi_k - \ddot{\bar{Y}}\cos\psi_k) = 0 \tag{20}$$

where $\bar{\omega}_\xi$ is the lead-lag frequency ratio, ψ_k is the azimuth angle, S_ξ is the first mass moment and I_ξ is the blade lead-lag

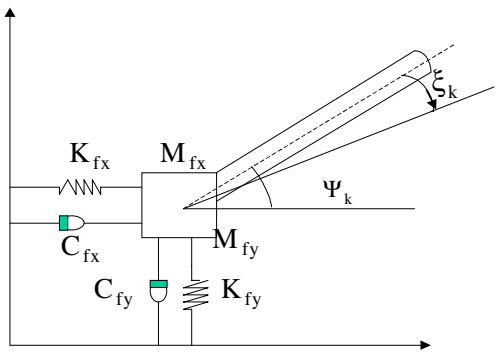

Figure 5. Schematic diagram of the classical ground resonance model.

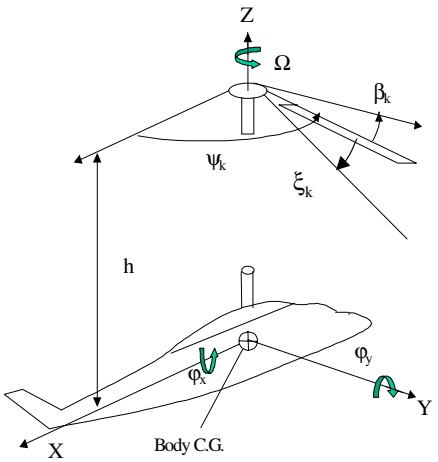

Figure 6. Schematic diagram of the air resonance model.

inertia. Quantities $\bar{X}$ and $\bar{Y}$ are dimensionless displacements of the hub center and η is the blade fundamental in-plane modal damping ratio. The quantity η is obtained from the eigensolution of the box beam with SCLs (equation (19)).

The air resonance model [19] is shown in figure 6. Only rigid body pitch and roll rotation degrees of freedom are taken into account in this model. A fundamental flap modal displacement (β_k) and a fundamental lead-lag modal displacement (ξ_k) are considered in this analysis. In figure 6, variables φ_x and φ_y represent the fuselage roll and pitch displacements, respectively. The center of gravity (CG) of the helicopter is assumed to lie in the rotor shaft. The distance from the CG to the hub center is h. The variable ψ_k is the azimuth angle. In this model, it is assumed that the blade mass is distributed uniformly along the blade span and the planform is assumed to be rectangular. It is also assumed that there is no geometric twist. The degree of freedom of the blade pitch is not included in the analysis. To further simplify the problem, the mode shapes are assumed to be straight lines and there is no structural coupling between the flap and lead-lag motions. The individual blade flap and lead-lag motions are combined together and are transferred to the non-rotating coordinate through multiblade transformation.

Similar to ground resonance analysis, the modal damping of the box beam with SCLs is calculated from equation (19) and is used in the blade flap and lead-lag equilibrium equations. In these equations, aerodynamic load is used as an external force vector acting on the rotor blades (see equation (27) below).

4. Aerodynamic forces

The aerodynamic forces are calculated based on a quasi-steady lifting line theory, combined with the Pitt dynamic inflow model [20]. Based on this model, the perturbation in the dimensionless induced velocity can be expressed as

$$v_1 = v_{10} + v_{1c}\bar{r}\cos\psi_k + v_{1s}\bar{r}\sin\psi_k \tag{21}$$

and

$$[\mathrm{M}]\begin{Bmatrix}\dot{v}_{10}\\ \dot{v}_{1s}\\ \dot{v}_{1c}\end{Bmatrix} + [\mathrm{L}]^{-1}\begin{Bmatrix}v_{10}\\ v_{1s}\\ v_{1c}\end{Bmatrix} = \begin{Bmatrix}\Delta C_T\\ C_L\\ C_M\end{Bmatrix} \tag{22}$$

$$[\mathrm{M}] = \begin{bmatrix}\frac{128}{75\pi} & 0 & 0\\ 0 & -\frac{16}{45\pi} & 0\\ 0 & 0 & -\frac{16}{45\pi}\end{bmatrix} \tag{23}$$

$$[\mathrm{L}] = \frac{1}{V}\begin{bmatrix}\frac{1}{2} & 0 & \frac{15\pi}{64}\sqrt{\frac{1-\sin\alpha}{1+\sin\alpha}}\\ 0 & -\frac{4}{1+\sin\alpha} & 0\\ \frac{15\pi}{64}\sqrt{\frac{1-\sin\alpha}{1+\sin\alpha}} & 0 & -\frac{4\sin\alpha}{1+\sin\alpha}\end{bmatrix} \tag{24}$$

where v_1, v_{10}, v_{1c} and v_{1s} represent perturbations in the total, the average, the cosine and the sine components of the induced velocity, respectively. The quantity $\bar{r}$ represents the blade radial station dimensionless by rotor radius. The quantity ψ_k denotes the azimuth angle of the ith blade, ΔC_T is the perturbation in the lifting force and C_L and C_M are the rolling and pitching moment coefficients, respectively. The matrix [M] is the apparent mass matrix, which reflects the influence of air mass inertia and [L] provides the static relationship between the induced velocity and aerodynamic loads.

Since the perturbation in the average induced velocity (v_{10}) does not couple with rotor flap, lead-lag, fuselage roll and pitch motion in hover, this term is neglected and only the terms v_{1c} and v_{1s} are included in the rotor–body coupled stability analysis. Therefore, equations (21) and (22) can be written for hover condition as

$$v_1 = v_{1c}\bar{r}\cos\psi_k + v_{1s}\bar{r}\sin\psi_k \tag{25}$$

$$\begin{bmatrix}\frac{16}{45\pi} & 0\\ 0 & \frac{16}{45\pi}\end{bmatrix}\begin{Bmatrix}v_{1s}\\ v_{1c}\end{Bmatrix} + \begin{bmatrix}v_s & 0\\ 0 & v_s\end{bmatrix}\begin{Bmatrix}v_{1s}\\ v_{1c}\end{Bmatrix} = -\begin{Bmatrix}C_L\\ C_m\end{Bmatrix} \tag{26}$$

where v_s is dimensionless equilibrium induced velocity in hover.

The sectional lift ($\mathrm{d}F_z$) and drag ($\mathrm{d}F_y$) on the ith blade can be written as

$$\begin{aligned}\mathrm{d}F_z &= \tfrac{1}{2}\rho ab(\theta U_T^2 - U_p U_T)\,\mathrm{d}r\\ \mathrm{d}F_y &= -\tfrac{1}{2}\rho ab(C_d U_T^2 - \theta U_p U_T - U_p^2)\,\mathrm{d}r\end{aligned} \tag{27}$$

where a is the blade section lift–curve slope, b is the blade chord, θ is the collective pitch and ρ is the density of air. The quantities U_T and U_p are the air velocities at blade sections perpendicular and tangent to the disk plane, respectively. These can be expressed as

$$\begin{aligned}U_T &= \Omega r - y'\\ U_p &= z' + v_0 + v_1\Omega R\end{aligned} \tag{28}$$

where v_0 is the induced velocity of the helicopter in equilibrium hover condition and z' and y' are the flap and lead-lag velocities, respectively. The rotor and fuselage properties are listed in appendix B.

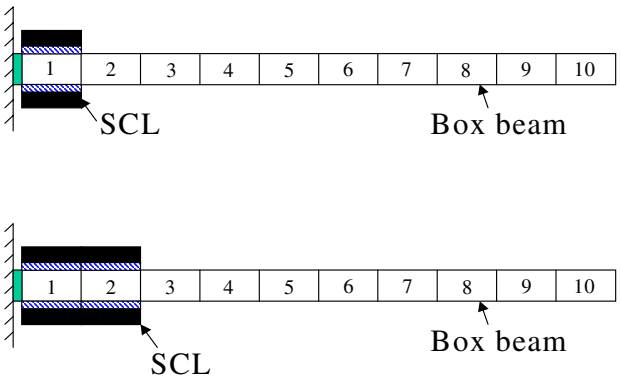

Figure 7. Illustration of box beams with one and two pairs of SCLs.

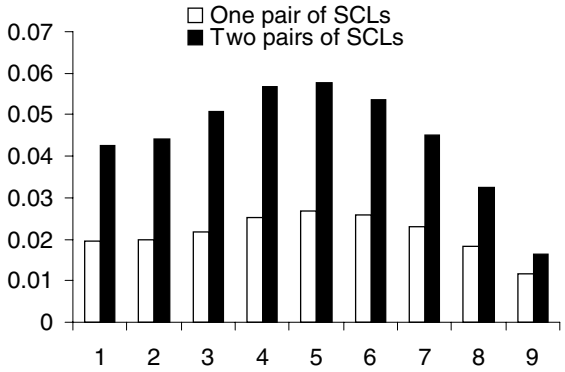

Figure 8. Variation of in-plane fundamental modal damping with location of SCLs.

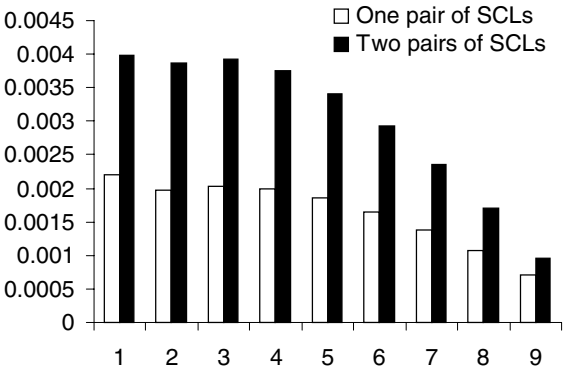

Figure 9. Variation of out-of-plane fundamental modal damping with location of SCLs.

5. Results and discussion

The aeromechanical behavior of a rotor blade built around the composite box beam, with top and bottom surface bonded SCLs, is studied in detail. Parametric studies are performed by varying the location and number of the SCLs. The rotor and fuselage properties are listed in appendices A and B. The dimensions of the box beam (figure 4) are such that length $L = 5.5$ m, width $a = 0.176$ m and high $b = 0.06$ m. Each wall is comprised of eight layers with thickness $t = 1$ mm. Two side walls are assumed to have the same stacking sequence $[45^\circ/45^\circ/45^\circ/45^\circ]_s$ and stacking sequence of the box beam upper and lower walls is $[-45^\circ/45^\circ/-45^\circ/45^\circ]_s$. In the SCL configuration (figure 3), the piezoelectric layer

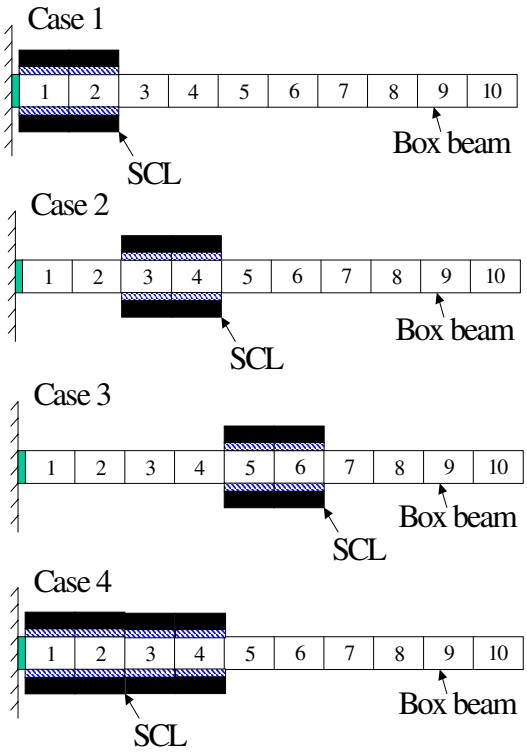

Figure 10. Schematic diagrams of the cases studied.

thickness (h_p) is 1 mm. The viscoelastic layer thickness (h_v) is 0.5 mm. Each SCL has the same width as that of the box beam. The box beam is discretized using 11 elements (including a root element, figure 7). The length of each SCL is the same as that of each element. The results are presented for two different SCL arrangements (figure 7). In the first, a single SCL pair is bonded to the top and bottom surfaces of one element of the box beam and in the second, two pairs of SCLs are surface bonded to cover two adjacent elements.

The in-plane and out-of-plane fundamental modal damping of the box beam in vacuum is analyzed first and their variations with changes in the locations of the SCLs are presented in figures 8 and 9. In these figures, the horizontal axis represents the locations of the SCL pairs. Figure 8 shows that significant in-plane modal damping is obtained with two pairs of SCLs. For example, two pairs of SCLs bonded on elements 1–2, 3–4 and 5–6 yield a modal damping ratio of 4.3%, 5.1% and 5.8%, respectively (see figure 8). The modal damping obtained with two pairs of SCLs located on elements 5 and 6 is 36% higher than the value obtained with two pairs of SCLs located closer to the root. A slight increase occurs when the locations are changed from elements 3 and 4 to elements 5 and 6. This indicates that more coupling between the lead-lag and torsion modes is achieved with the SCLs placed over the midspan of the beam. This can be explained as follows. The combined effect of high-frequency modes and centrifugal force results in the midspan locations of SCLs for maximizing lead-lag damping. Figure 9 shows that the out-of-plane fundamental modal damping decreases as the SCLs move from the root elements to tip elements of the box beam. This is because the out-of-plane modal strain is largest at the root region. Also, as seen from figures 8 and 9 the modal damping increases, for both in-plane and out-of-plane motion, with an increase in the number of bonded SCLs.

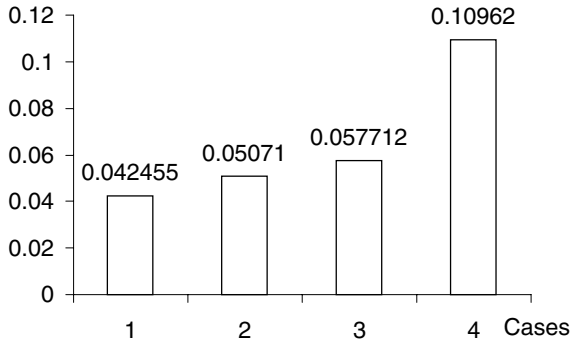

Figure 11. In-plane fundamental modal damping ratio.

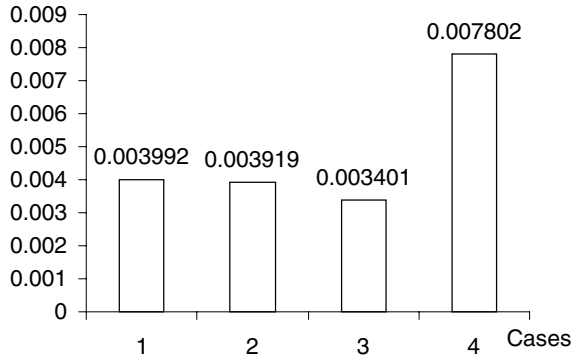

Figure 12. Out-of-plane fundamental modal damping ratio.

A total of four cases (figure 10), based on the number and locations of the SCLs, are investigated for helicopter aeromechanical stability analysis. The size of each pair of SCLs is the same as that of the SCLs used above. The in-plane and out-of-plane fundamental modal damping of the box beam in vacuum are presented in figures 11 and 12 for all four cases. In these figures, numbers 1–4 correspond to the four different cases studied shown in figure 10.

The results for the ground resonance model are shown in figures 13–15. In figure 13, coupled rotor–body frequencies are presented for the four system modes; lead-lag regressive mode (LR), lead-lag advancing mode (LA), fuselage lateral mode (By) and longitudinal mode (Bx). In this figure, ω is the ground resonance frequency, Ω is the rotor angular velocity and Ω_0 is the rotor normal angular velocity. As seen from this figure, without rotor and fuselage damping, the lead-lag frequency coincides with the fuselage frequency leading to ground resonance.

The variation in the ground resonance modal damping with rotor rotational speed is presented in figure 14 for both the reference case (no SCL) and case 1 (two pairs of SCLs located in the root region) with 20% fuselage critical damping. The LR mode is unstable in the reference case (without SCL and fuselage damping). However, with two pairs of SCLs, the coupled system becomes stable with LR modal damping of about 0.023. It must be noted that the regressive mode is usually the most unstable mode in ground resonance stability analysis.

Figure 15 shows the LR modal damping for cases 1–4. A fuselage critical damping of 25% is assumed in these cases. All four cases lead to stable coupled rotor–body systems as shown in this figure. As two pairs of SCLs are moved from the root elements towards the midspan, the LR modal damping increases as expected. In case 4, a larger LR modal damping of about 0.05 is achieved due to the increase in the number of segmented SCLs.

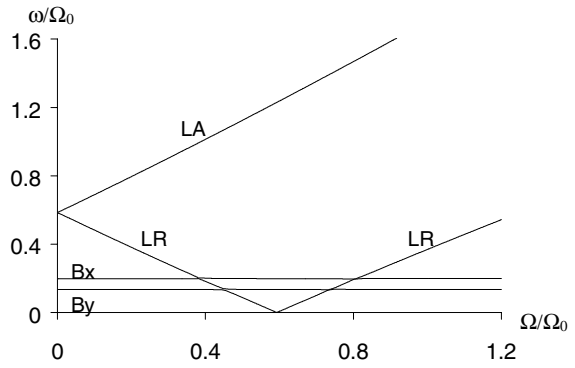

Figure 13. Variation of ground resonance modal frequencies with rotor rotational speed (case 1).

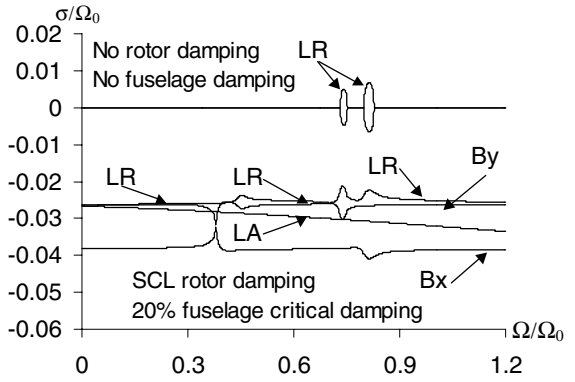

Figure 14. Variation of ground resonance modal damping with rotor rotational speed (case 1).

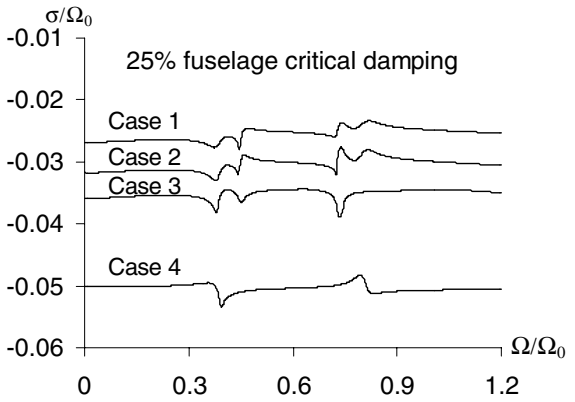

Figure 15. Comparisons of regressive lead-lag modal damping (cases 1–4).

To understand the significance of the results obtained, it is necessary to examine the relationship between the minimum mechanical rotor lead-lag critical damping ratio (n_b) and fuselage equivalent critical damping ratio (n_f) [25]. Assuming that the equivalent lateral stiffness, damping and mass of the fuselage are equal to the corresponding longitudinal values, the following expressions for critical

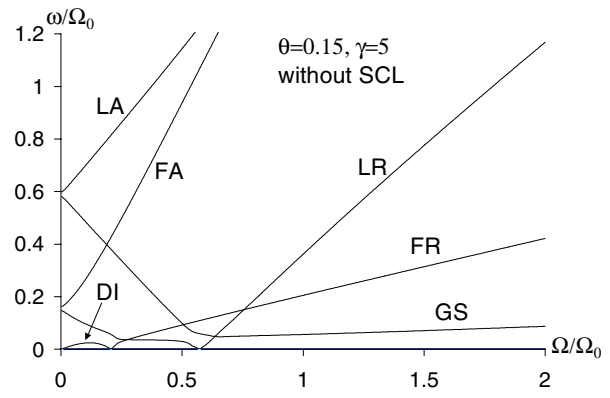

Figure 16. Variation of modal frequencies of air resonance with rotor rotational speed.

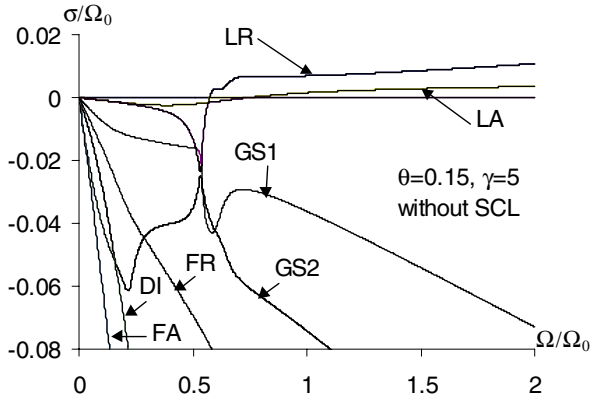

Figure 17. Variation of modal damping of air resonance with rotor rotational speed.

coupled rotor–body system stability can be obtained:

$$4n_b n_f = \frac{3\mu(1-\bar{\omega}_\xi)^3}{8\bar{\omega}_\xi} \qquad \mu = \frac{2NS_\xi}{M_x} = \frac{2NS_\xi}{M_y} \tag{29}$$

where μ is the ratio of blade first mass moment to the mass of the fuselage and $\bar{\omega}_\xi$ is the lead-lag frequency. As seen from equation (29), for given values of μ and ω_ξ, with an increase in the body equivalent damping, the required amount of the lead-lag damping ratio reduces. Hence, the actual system will be more stable than the results presented in this paper since helicopters have overdamped fuselage landing gear systems.

The results of the air resonance stability analysis are presented in figures 16–21. In figure 16, the coupled rotor–body system frequencies are shown for the seven system modes: (LR), (LA), flap regressive mode (FR), flap advancing mode (FA), gyroscopic mode (GS), dynamic inflow mode (DI) and zero root modes. The results are presented for lock number $\gamma = 5$ and collective pitch $\theta = 0.15$ and $\theta = 0.3$. As seen from figure 17 with a collective pitch $\theta = 0.15$, the system is unstable in the absence of rotor mechanical lead-lag damping. The unstable modes are the LR and the LA modes, the LR mode being more unstable in this case. With the application of SCLs to the coupled system, stability is ensured as shown in figure 18. A modal damping of 0.028 is obtained for the LR mode in case 3 at regular rotational speed. As the locations of two pairs of SCLs are moved towards the midspan, the LR modal damping increases. Case 3 yields the largest modal damping. As expected, a much larger modal damping is obtained in case 4 with an increase in the number of SCLs (figure 19)

Normally, with an increase in the collective pitch, θ, the instability and the unstable domain of the LR mode and LA mode increase. Figure 20 shows that the LR mode is still very close to the unstable region over a 0.75–1.0 rotor rotational speed ratio when only two pairs of SCLs (case 1) are used. A stable system is achieved and is guaranteed over the entire speed regime in cases 1–3.

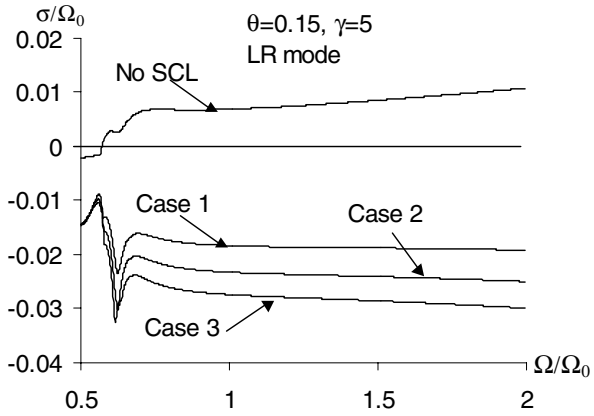

Figure 18. Variation of LR modal damping with rotor rotational speed (cases 1–3).

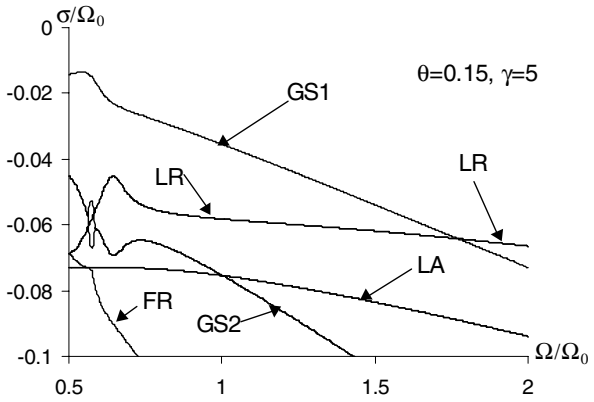

Figure 19. Variation of modal damping with rotor rotational speed (case 4).

6. Concluding remarks

The use of SCL passive damping on helicopter aeromechanical stability, including ground and air resonance, is investigated. The principal load-carrying member in the rotor blade is represented by a composite box beam with SCls bonded on the top and bottom surfaces of the beam. A finite-element model is developed for the analysis of the box beam using hybrid displacement fields. The higher-order displacement field is used in the composite box beam to capture the transverse shear deformations. Next, a ground resonance model and an air resonance model are developed. A linear dynamic inflow model is used in the air resonance analysis. Parametric studies are conducted by varying the number and

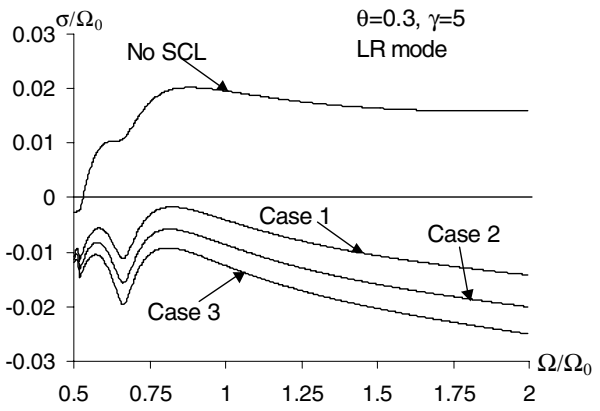

Figure 20. Variation of LR modal damping with rotor rotational speed (cases 1–3).

Table 1. Material properties of PZT and graphite/epoxy composite.

	PZT	Viscoelastic layer	Graphite/epoxy
E_{11} (GPa)	63	25	144.23
E_{22} (GPa)	63	25	9.65
E_{33} (GPa)	63	25	9.65
G_{23} (GPa)	24.6	10	3.45
G_{13} (GPa)	24.6	10	4.14
G_{12} (GPa)	24.6	10	4.14
ν_{12}	0.28	0.25	0.3
ν_{23}	0.28	0.25	0.3
ν_{31}	0.28	0.25	0.02
Density (kg m^{-3})	7600	1600	1389.23
Piezoelectric Constant (pm V^{-1})	254		
VEM			
Ω (rad s^{-1})		20	
C		1.2	

locations of the SCLs along the blade span. The following important observations are made from the current study.

(1) Significant in-plane fundamental modal damping is obtained for the box beam in vacuum with segmented SCLs.

(2) Out-of-plane modal damping decreases as the locations of the SCLs move from the root elements to the tip elements of the box beam.

(3) The use of SCLs yields significant improvements in both the ground and the air resonance aeromechanical stability.

(4) Locations of the SCLs play a very important role. Larger in-plane modal damping is achieved when the SCLs are located closer to the blade midspan driven by increased modal damping.

Acknowledgment

The research was supported by the US Army Research Office, grant number DAAH04-96-1-0163, technical monitor Gary Anderson.

Appendix A. Parameters for ground resonance model

Blade first mass moment $S_\xi/I_\xi = 1.5$.
Equivalent fuselage mass $M_x = M_{fx} + NM_b$.
Equivalent fuselage mass $M_y = M_{fy} + NM_b$.
Fuselage frequency $\omega_x = \sqrt{\frac{K_{fx}}{M_x}} = 7.94$.
Fuselage frequency $\omega_y = \sqrt{\frac{K_{fy}}{M_y}} = 5.58$.
Ratio of blade first mass moment to fuselage mass:
$\mu_x = 2NS_\xi/M_x = 0.0708$.
$\mu_y = 2NS_\xi/M_y = 0.112$.
Blade number $N = 4$.
Rotor radius $R = 5.5$ m.
Rotor normal angular velocity $\Omega_0 = 37.5$ s^{-1}.
Fundamental lead-lag frequency ratio
$\bar{\omega}_\xi = 0.62$ ($\Omega = \Omega_0$).

Appendix B. Parameters for air resonance model

Blade first mass moment $S_\xi/I_\xi = 1.5$.
Blade number $N = 4$.
Fuselage roll and pitch inertia:
$\bar{I}_x = (I_{fx} + h^2 NM_b)/\frac{N}{2} I_b R^2 = 2.86$
$\bar{I}_y = (I_{fy} + h^2 NM_b)/\frac{N}{2} I_b R^2 = 9.42$.
Rotor normal angular velocity $\Omega_0 = 37.5$ s^{-1}.
Fundamental flap and lead-lag frequency ratio:
$\bar{\omega}_\xi = 0.62$ ($\Omega = \Omega_0$)
$\bar{\omega}_\beta = 1.08$ ($\Omega = \Omega_0$).
Blade airfoil profile lift–curve slop $a = 2\pi$.
Blade airfoil drag coefficient $C_d = 0.01$.
Distance from body CG to rotor plane $h/R = 0.312$.

References

[1] Park C and Chopra I 1994 Modeling piezoceramic actuation of beams in torsion *35th Structures, Structural Dynamics and Materials Conf. and Adaptive Structures Forum, (Hilton Head, NC, April 18–21, 1994)*

[2] Chopra I 1993 Development of a smart rotor *19th Eur. Rotorcraft Forum (Cernobbio, Italy, September 14–16, 1993)* Paper No N6

[3] Spangler R L Jr and Hall S R Piezoelectric actuators for helicopter rotor control *AIAA-90-1076*

[4] Ben-Zeev O and Chopra I 1995 Advanced in the development of an intelligent helicopter rotor employing smart trailing-edge flaps *SPIE North American Conf. on Smart Structures and Materials (February 27–March 3, 1995)*

[5] Chattopadhyay A, Liu Q and Gu H 1998 Aeromechanical modeling of smart composite rotor blade for vibration reduction *53rd Annual Forum of the American Helicopter Society (Washington DC, May 29–31, 1998)*

[6] Chattopadhyay A, Liu Q and Nam C Rotor vibratory response analysis using smart materials and aeroelastic control *AIAA-99-1504*

[7] Peters D A, Boyd D D and He C J 1989 Finite-state induced-flow model for rotor in hover and forward flight *J. Am. Helicopt. Soc.* **34**

[8] Baz A and Ro J 1993 Partial treatment of flexible beams with active constrained damping *Conf. of the Society of Engineering Science (ASME-AMD) (Charlottesville, VA)* vol 167 pp 61–8

[9] Baz A and Ro J Finite element modeling and performance of active constrained layer damping *Proc. 9th VPI and SU Conf. Dynamics and Control of Large Structures (Blacksburg, VA)* pp 345–58
[10] Ro J and Baz A 1996 Optimum design and control of active constrained layer damping *J. Mech. Design* and *J. Vib. Acoust.* (special combined edition) **117** 135–44
[11] Lesieutre G A and Lee U 1996 A finite element for beams having segmented active constrained layers with frequency-dependent viscoelastics *J. Smart Mater. Struct.* **5** 615–27
[12] Badre-Alam A, Wang K W and Gandhi F 1999 Optimization of enhanced active constrained layer (EACL) treatment on helicopter flexbeam for aeromechanical stability augmentation *Smart Mater. Struct.* **8** 182–96
[13] Liu Y and Wang K W 1999 A non-dimensional parametric study of enhanced active constrained layer damping treatments *J. Sound Vib.* **234** 611–44
[14] Gu H, Chattopadhyay A and Nam C Modeling segmented active constrained layer damping using hybrid displacement field *AIAA 99-1542*
[15] Azvine B, Tomlinson G R and Wynne R J 1995 Use of active constrained-layer damping for controlling resonant vibration *J. Smart Mater. Struct.* **4** 1–6
[16] Liao W H and Wang K W 1995 On the active–passive hybrid control actions of structures with active constrained layer treatment *Proc. ASME 15th Biennial Conf. on Mechanical Vibration and Noise* ASME DE vol 84–3 pp 125–41.11
[17] Liao W H and Wang K W 1996 A new active constrained layer configuration with enhanced boundary actions *J. Smart Mater. Struct.* **5** 638–48
[18] Chattopadhyay A, Liu Q, Gu H and Zhou X Dynamics of a composite box beam with segmented active constrained layer damping in preparation
[19] Zhang X 1986 Physical understanding of helicopter air and ground resonance *J. Am. Helicopt.* **31**
[20] Pitt D M and Peters D A. 1981 Theoretical predictions of dynamic inflow derivatives *Vertica* **5**
[21] Ormiston R A, Saberi H and Anastassiades T 1995 Application of 2GCHAS to the investigation of aeromechanical stability of hingless and bearingless rotor helicopters *Proc. Conf. on the 51st Forum of the American Helicopter Society (Fort Worth, TX, May 9–11, 1995)*
[22] Gandhi F and Chopra I 1994 Analytical model for a nonlinear elastomeric lag damper and its effect on aeromechanical stability in hover *J. Am. Helicopt.* **38**
[23] Bousman W G 1981 An experimental investigation of the effects of aeroelastic couplings on aeromechanical stability of a hingless rotor helicopter *J. Am. Helicopt.* **26**
[24] Lesieutre G A and Mingori D L 1990 Finite element modeling for frequency dependent materials using augmenting thermodynamic fields *J. Guid. Control* **13** 1040–50
[25] Johnson W 1980 *Helicopter Theory* (Mineola, NY: Dover)